Effect of surfactants during drop formation in a microfluidic channel: A combined experimental and CFD approach

M. Kalli, P. Pico, L. Chagot, L. Kahouadji, S. Shin, J. Chergui, D. Juric, O.K. Matar, P. Angeli

Effect of surfactants during drop formation in a microfluidic channel: A combined experimental and CFD approach

M. Kalli[1], P. Pico[2], L. Chagot[1], L. Kahouadji[2], S. Shin[3], J. Chergui[4], D. Juric[4,5], O. K. Matar[2]† and P. Angeli[1]†

[1]Chemical Engineering Department, University College London, Torrington Place, London WC1E 7JE, United Kingdom

[2]Department of Chemical Engineering, Imperial College London, South Kensington Campus, London SW7 2AZ, United Kingdom

[3]Department of Mechanical and System Design Engineering, Hongik University, KR

[4]Université Paris Saclay, Centre National de la Recherche Scientifique (CNRS), Laboratoire Interdisciplinaire des Sciences du Numérique (LISN), 91400 Orsay, France

[5]Department of Applied Mathematics and Theoretical Physics, University of Cambridge, Cambridge CB3 0WA, UK

(Received xx; revised xx; accepted xx)

The effect of surfactants on the flow characteristics during rapid drop formation in a microchannel is investigated using a combination of high-speed imaging, micro-particle image velocimetry (μPIV), and numerical simulations; the latter are performed using a three- dimensional multiphase solver that accounts for the transport of soluble surfactants in the bulk and at the interface, and adapted to the context of a hybrid Front-Tracking/Level-set method. Drops are generated in a flow-focusing, cross- junction microchannel, using silicone oil (4.6 mPa s) as the continuous phase and an aqueous mixture of 52% w/w glycerol as the dispersed phase. A non-ionic surfactant (Triton X-100) is dissolved in the dispersed phase at concentrations below and above the critical micelle concentration (CMC). Excellent agreement between the numerical predictions and the experimental data is found for the drop size, drop formation time, velocity and circulation patterns. The results reveal strong circulation patterns in the forming drop in the absence of surfactants, whose intensity decreases with increasing surfactant concentration, while a stagnation point is found just at pinch-off. The surfactant concentration profiles in the bulk and at the interface are shown for all stages of drop formation. It is found that the surfactant interfacial concentration is large at the front of the forming drop and at the back, while the neck region is almost surfactant-free. Within the forming drop, the surfactant is mainly concentrated in the middle. Marangoni stresses develop but away from the neck, contributing mainly to changes in the velocity profile inside the drop.

Key words: Droplet formation, Flow-focusing microchannel, Surfactants, μPIV

1. Introduction

Microfluidic channels are widely used to produce droplets with controlled size and low polydispersity index, which are important in applications such as emulsification,

† Email address for correspondence: p.angeli@ucl.ac.uk, o.matar@imperial.ac.uk

inkjet printing, cosmetics, and healthcare (Lawrence & Rees 2000; Yang *et al.* 2018; Park *et al.* 2021). Surfactants are commonly added during drop formation to modify the interfacial properties and improve the stability of the emulsions. The presence of surfactant molecules significantly affects the non-linear drop formation process and thus the final size (Chen *et al.* 2015). In the common dripping regime, drop formation depends on the balance between the interfacial tension and the drag forces, with the latter being the combination of shear and pressure forces (Xu *et al.* 2006). As a result, a lower interfacial tension caused by surfactant addition will result in smaller and more rapidly-forming drops. As seen in previous work, the small characteristic timescales that are present in microfluidics can lead to interfacial tension values different from the equilibrium ones, which are often used in the calculation of capillary numbers Ca (Kalli & Angeli 2022) and in predictive equations for drop size. Additionally, shear stresses from high continuous phase velocities can redistribute surfactant molecules at the interface, which will cause interfacial tension gradients and thus Marangoni stresses (Kovalchuk & Simmons 2021). For surfactants that result in a large decrease in interfacial tension, the effect of interface retardation at low surfactant concentrations can be sufficiently large to change the velocity fields close to the interface and inside the drop, due to Marangoni stresses in the opposite direction to the flow. At high concentrations, surfactant exchange between the bulk and the interface is fast and interface remobilisation is seen at high velocities (Martin & Hudson 2009). Since both observations will greatly impact the final surfactant transport, it is important to study the behaviour of such surfactants at different concentrations, below and above the critical micelle concentration (CMC).

As first reported by Garstecki *et al.* (2005), drop formation in the dripping regime is typically divided into three stages called expansion, necking, and pinch-off. Following drop detachment, the interface pulls towards the inlet before recoiling in the downstream direction. At this stage, drop growth is mainly in the streamwise direction forming a parabolic interface profile and is dominated by interfacial tension. Once the pressure builds-up due to restriction of the inlet from the forming drop, the drag force overcomes the interfacial tension force and a reversal of the interface curvature is observed, which indicates the beginning of the necking stage. The neck width decreases until the drag force is large enough to cause drop detachment and thus pinch-off. In recent studies (Wang *et al.* 2009; Xu *et al.* 2012), it was found that high dispersed phase flowrates enhance convection and surfactant mass transfer to the interface, which explain the reduced interfacial tension values at short formation times. Furthermore, it was found that absorption and mass transfer rates can compete with drop formation times (Kalli *et al.* 2022). Investigating the transport of surfactants during each phase of the drop formation process is vital in understanding the impact on the final drop size.

Improvements in experimental techniques allow the accurate visualisation of flows inside microchannels, which can be used to explore the effects of surfactant transport. Kiratzis *et al.* (2022) used Ghost Particle Velocimetry (GPV) to study the effect of surfactant concentration, continuous phase velocity and viscosity on drop formation in rectangular channels. Results revealed smaller velocities at the interface when a surfactant of the same family but with a slower adsorption rate (lower CMC) was present, suggesting the presence of Marangoni stresses. In addition, larger internal circulation inside the drops was seen at higher continuous phase viscosity during the expansion stage. Roumpea *et al.* (2019) used an innovative two-colour micro-Particle Image Velocimetry (μPIV) technique to study velocity fields in a flow-focusing microchannel in the presence of two cationic surfactants of the same family but different adsorption kinetics (C_{12}TAB, dodecyltrimethylammonium bromide and C_{16}TAB, hexadecyltrimethylammonium bromide). Addition of surfactant in the dispersed phase resulted in higher velocities at the tip

and more uniform velocity fields inside the drop, which was attributed to surfactant accumulation at the tip that increases the interface rigidity in that area. A second observation was the decrease in the circulation inside the drop, which was again attributed to Marangoni effects that caused the interface to move in the opposite direction to the flow and opposed circulation. Similar effects were seen when a non-ionic surfactant (Span80) was added in the continuous oil phase, in a T-junction channel (Riaud *et al.* 2018). A stagnant cap was observed in this case near the drop tip that split the forming drop interface into a mobile and a rigid region. The resulting Marangoni force in the opposite direction of the forming drop resisted the flow circulation. Studies on drop formation in a flow-focusing microchannel by Carrier *et al.* (2015) revealed a flow inversion during pinch-off and weaker recirculation at the base of the drop compared to its front, upon addition of SDS (sodium dodecylsulfate) surfactant. Changes in circulation within surfactant-laden drops using μPIV were investigated in emulsions produced in a tapered microchannel leading to a geometrical constriction (Leong *et al.* 2016). It was found that vortical structures forming when the drops passed the constriction, increase circulation up to 2.5 times compared to droplet mixing at the channel constriction.

Despite the work reviewed above, there are still important limitations to be addressed in order to fully understand the effect of surfactant on the drop formation process. As previously mentioned, it is essential to know the surfactant distribution at the interface as it can accumulate at the tip and cause Marangoni flows as the drop forms. The surfactant concentration at the interface is very challenging to obtain experimentally (Dussaud *et al.* 2005), especially during flow. Even if a fluorescent surfactant is used, the powerful intensity of the laser needed for visualisation can cause photobleaching (Eggeling *et al.* 1998), which is non-reversible. Another issue is self-quenching (Aicolina *et al.* 1989; Li *et al.* 2022), where the total emitted intensity can change upon temperature, pressure, or pH fluctuations. Additionally, most fluorescent surfactants are soluble in solvents such as chloroform and dimethylformamide, which can be toxic. Since most fluorescently-tagged surfactants are synthesised by adding a fluorescent group to the amphiphilic structure of the surfactant, they usually result in heavier molecules that exhibit low interfacial activity (i.e. small reduction in interfacial tension with concentration) or slow adsorption kinetics, especially when compared with the fast drop formation process. Dong *et al.* (2019) used Planar Laser Induced Fluroescence (PLIF) to capture the spatio-temporal distribution of a fluorescent surfactant during the coalescence of a mm size drop with a flat surface, using a laser sheet with 1 mm thickness. This dimension is an order of magnitude larger than typical microchannel length scales. On the other hand, the volume illumination used for microchannel LIF studies is not ideal when tracing molecules at a 3D interface.

The complex phenomena of drop formation in microchannels have also been investigated through numerical approaches. Computational Fluid Dynamics (CFD) simulations in particular are a powerful tool to overcome most of the above-mentioned experimental limitations and extract useful information related to the dynamics of the flow. Numerous CFD investigations based on Volume-of-Fluid (VOF) and Level-Set methods have been conducted to determine the role of operating conditions on the drop formation process in surfactant-free systems. These studies have revealed the interplay between capillarity, inertia, and viscosity for different microfluidic junction geometries and their effects on drop formation (Li *et al.* 2012; Lan *et al.* 2014; Soh *et al.* 2016; Ngo *et al.* 2015; Kahouadji *et al.* 2018; Filimonov *et al.* 2021; Van der Graaf *et al.* 2006; Zhao *et al.* 2015). Recent studies in the presence of surfactants have provided a detailed description of the heterogeneous distribution of surfactant concentration at the interface and the effect on drop formation time and drop size. Riaud *et al.* (2018) performed numerical simulations

inside a T-junction microchannel for a Span80-octane/water mixture and compared the results against μPIV experiments. The authors found that the interfacial distribution of surfactants on growing droplets is not uniform but surfactants tend to concentrate at the droplet tip. They also reported that surfactant adsorption is faster than drop formation at low velocities and low Ca. As Ca is increased, either by lowering the interfacial tension or by increasing the inlet velocity, the characteristic drop formation time is reduced and thus adsorption becomes slower than formation time. The authors showed that droplet volume increases with increasing dispersed phase flowrate and decreasing Ca; both parameters are therefore necessary to predict the drop size. Jin *et al.* (2006) studied the effect of soluble surfactants on drop necking and used a nonlinear model to relate interfacial tension to surfactant concentration at the interface, by accounting for maximum surfactant packing at the interface. The analysis revealed that a family of necks formed, as a result of a primary and a secondary thinning rate of the neck, depending on the local accumulation of surfactants, and demonstrated that drop detachment behaviour can be used to quantify surfactant dynamics. Antonopoulou *et al.* (2021) performed experimental and numerical studies on the flow behaviour during inkjet printing and explained the effect different surfactants have on pinch-off during jetting.

This paper combines unique experimental and numerical approaches to investigate surfactant transport in the bulk, distribution at the interface and Marangoni phenomena during the fast drop formation process in a microfluidic channel. A non-ionic (CMC_{TX100} = 3.5mM) surfactant is used in the dispersed aqueous phase at concentrations below and above the CMC. A novel high-speed μPIV system is able to follow all stages of the fast drop formation process, which is a key improvement compared to previous works (Riaud *et al.* 2018; Roumpea *et al.* 2019). The CFD simulations include the exchange of surfactant between the bulk of the drop and the interface, as opposed to previous works that considered only transport at the interface (Antonopoulou *et al.* 2021; Riaud *et al.* 2018). The effect of surfactant on the vortical structures and velocity fields are discussed for the different stages of drop formation. The CFD simulations provide information on surfactant concentrations at the interface that cannot be obtained experimentally. In addition, they reveal the vortical structures very close to the interface where measurements are not accurate because of the low concentration of the PIV tracer particles in this region (i.e. at the neck region just before pinch-off). They also enable investigations of the drop in three dimensions, which are very challenging to obtain experimentally. The experiments on the other hand provide data on the effect of the surfactant at high concentrations above the CMC, which is beyond the capabilities of the current model. The Marangoni stresses at the interface are calculated and presented as a function of time and space for the first time during the whole drop formation process.

2. Experimental Methods

2.1. *Droplet generation*

The experiments were performed in a glass flow-focusing microchannel from Dolomite Microfluidics (Part No. 3000436) already used in previous works (Roumpea *et al.* 2019; Kovalchuk *et al.* 2018). At the cross-junction the inlet dimensions are 195 μm $\times$ 190 μm (width $\times$ depth) and the dimensions of the main channel are 390 μm $\times$ 190 μm (width $\times$ depth). The continuous phase was introduced via the side channels and then the aqueous phase via the central channel of the junction (see figure 1a). For all configurations, silicone oil (Clearco, density: ρ_c = 920 kg m^{-3}, viscosity: μ_c = 4.6 mPa s at 20°C) was used as the continuous phase and a mixture of 52% w/w glycerol and 48% w/w water

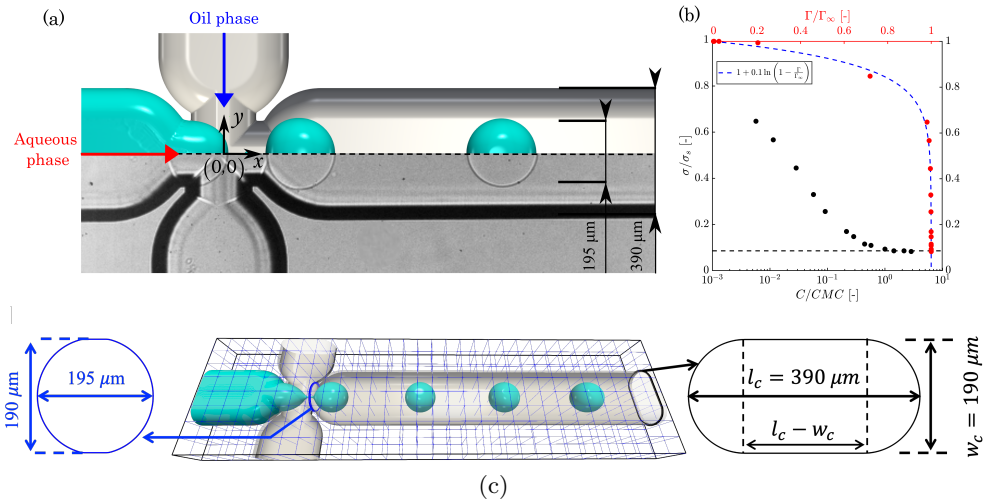

FIGURE 1. (a) Numerical configuration, and an illustrative snapshot of a top-view of the interface (top), and the corresponding high-speed image from experiments (bottom); (b) interfacial tension isotherm for TX100 surfactant showing the variation of equilibrium interfacial tension , σ. Black points represent σ (normalised by the surfactant-free value of interfacial tension, σ_s) with the semi-log variation of the surfactant bulk concentration C (normalised by the CMC). Red points represent the interfacial surfactant concentration, Γ (normalised by its saturation value, Γ_∞) obtained using Eq. (3.7). The blue dashed line represents the fitting of $\sigma/\sigma_s = 1 + 0.1\ln(1 - \Gamma/\Gamma_\infty)$; (c) geometrical details of the microfluidic channel decomposed into $240 = 30 \times 8 \times 1$ subdomains. Each subdomain contains a equal and structured mesh resolution of 32^3, for a total of $960 \times 256 \times 32$ cells.

(Sigma Aldrich, $\geqslant$99.5%, density: $\rho_d = 1132$ kg m^{-3}, viscosity $\mu_d = 6.8$ mPa s at 20°C) with and without surfactant was selected as the dispersed phase. Based on the work of Kalli *et al.* (2022), the flowrates were selected to form drops in the dripping regime. Using syringe pumps (KDS Scientific, $\pm$ 5 $\times 10^{-9}$ mL min $^{-1}$), the continuous phase was introduced with a total flowrate $Q_c = 0.12$ mL min^{-1}, while the dispersed phase had a flowrate of $Q_d = 0.01, 0.02$ mL min^{-1}. To observe the impact of interfacial tension on the drop formation, several concentrations of the non-ionic surfactant Triton X-100 (TX100), (Acros organics, $M_w = 646.85$ g/mol, $\geqslant$95%) were dissolved in the dispersed phase at concentrations of $(0.1, 0.2, 0.6, 1.0, 1.4, 2.1, 2.9, 4.3, 5.7, 8.6) \times$ CMC. Figure 1(b) shows the equilibrium interfacial tension values (σ), normalised by the final equilibrium interfacial tension value at CMC = 3.5mM ($\sigma_{\Gamma=\Gamma_\infty} = 2.9$ mN/m) as measured using a Du Noüy ring attached to a Force K100 Tensiometer (Krüss GmbH).

2.2. *Optical techniques*

The experimental setup is shown in figure 2. Two different illumination modes were used for the micro Particle Image Velocimetry (μPIV) or the High-Speed Imaging (HSI). To allow full optical access for all measurements and avoid optical distortions, in particular close to the channel wall, both phases were selected to match the refractive index of the glass microchannel ($n_i = 1.39$). For both modes, the images were taken with a 12-bit high-speed camera (Phantom v1212, 1280×800 pixels resolution). In the HSI experiments, the acquisition frequency was 10 000 Hz and the camera was equipped with a Nivatar $\times$20 zoom lens and an LED backlight for illumination. Results were averaged for at least 15 drops (drop size polydispersity $\leqslant$ 1.2%). The experimental error is 3 μm per pixel for the spatial resolution and 0.1 ms for the time resolution.

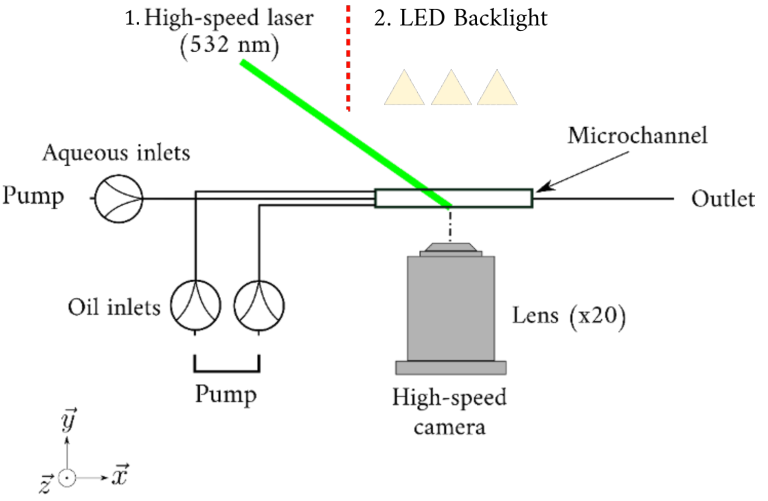

FIGURE 2. Experimental setup of the HSI and μPIV techniques.

The high-speed μPIV experiments were performed by switching modes from the LED light (2) to the laser source (1) as shown in figure 2. The laser illumination was generated with a high-speed 60W pulsed Nd-Yag (Litron), which allows the observation in time of the droplet generation. The dispersed phase was seeded with 1 μm carboxylate-modified microspheres FluoSpheres, with an absorbance of 542 nm and an emission of 612 nm. For the PIV image pairs, the camera was equipped with a $\times 20$ microscope lens (Mitutoyo Ltd) and focal depth of 1.6 μm. The lens was mounted with a high-pass filter (> 565 nm) to eliminate reflections from the channel walls. Moreover, to be able to follow the interface during the PIV measurements, a small amount of rhodamine B (with absorbance of 510 nm and emission of 610 nm) was added in the dispersed phase (0.05 ppm). The high-speed μPIV allows measurements in the channel centre during drop formation, which follow the whole process from the expansion $t = t_{exp}$ to the pinch-off stage $t = t_{pin}$. For each measurement, 2 000 image pairs were acquired at a frequency of 3 000 Hz which represent $\sim$20 drop formation cycles. The measurements were performed in the entire channel width ($y/l_c \in [-1, 1]$, with y the transverse direction) and around the droplet emergence area ($x/l_c \in [-2, 2]$, with x the streamwise direction). The local coordinate system is defined in figure 1(a) where $(x, y) = (0, 0)$ is the center of the cross junction. All velocity fields were computed with the free PIV software CPIV-IMFT developed at IMFT. It is based on an FFT cross-correlation method with peak-locking reduction schemes and parallelisation. In the processing, 16 $\times$ 16 pixels interrogation boxes and 50% overlap were used, yielding a grid resolution of 1.4 μm.

3. Numerical formulation, scaling, and validation

3.1. *Numerical formulation and problem statement*

As mentioned in §2, the microfluidic channel used in this study consists of a combination of both cross-junction and flow-focusing devices. Its computational representation and dimensions are illustrated in figure 1(c). The four branches of this device are identical with an oval cross-section shape of length $l_c = 390$ μm and width $w_c = 190$ μm. This cross-section is comprised of a rectangular piece of dimensions $w_c \times (l_c - w_c)$ connected to two semicircles of diameter w_c. Figure 1(c) also shows the three-dimensional

computational domain and its decomposition into $240 = 30 \times 8 \times 1$ sub-domains used for the Message Passing Interface (MPI) computing protocol. The numerical construction of this device follows a similar approach as that used in Kahouadji *et al.* (2018). This approach bypasses the typical obstacles in construction and meshing that arise when handling complex geometries by employing a static distance function for several primitive objects (e.g., cylinders, planes, and tori), and simple algebraic operations between them, such as "union" and "intersection".

The flow is considered incompressible and both the continuous and dispersed phases are assumed to be Newtonian. The following scaling is adopted to non-dimensionalise the equations governing the flow dynamics coupled to the surfactant transport in the bulk of the dispersed phase and at the interface:

$$\tilde{\mathbf{x}} = \frac{\mathbf{x}}{l_c},\ \tilde{\mathbf{u}} = \frac{\mathbf{u}}{U_{sc}},\ \tilde{t} = \frac{t}{l_c/U_{sc}},\ \tilde{p} = \frac{p}{\mu_c U_{sc}/l_c},\ \tilde{\sigma} = \frac{\sigma}{\sigma_s},$$
$$\tilde{\Gamma} = \frac{\Gamma}{\Gamma_\infty},\ \tilde{C} = \frac{C}{CMC},\ \tilde{C}_s = \frac{C_s}{CMC}. \tag{3.1}$$

Here, the tildes designate dimensionless quantities, and $\mathbf{x}$, t, $\mathbf{u}$, and p are the spatial coordinate, time, velocity, and pressure, respectively; the interface surfactant concentration is represented by Γ, C and C_s are the concentrations at the bulk and the bulk sub-phase, located immediately adjacent to the interface, respectively (Shin *et al.* 2018), and σ is the local interfacial tension varying as function of Γ. The length scale l_c, the average surface velocity of the continuous phase in the main portion of the channel, $U_{sc} = Q_c/A$ ($A = l_c w_c + (\pi/4 - 1)\, w_c^2$), the interfacial tension in a surfactant-free system, σ_s, the saturation interfacial concentration, Γ_∞, and the CMC, are used as the characteristic length, velocity, interfacial tension, and interfacial and bulk surfactant concentration scales, respectively; ρ_c and μ_c are the continuous phase density and dynamical viscosity, respectively. The dimensionless governing equations for the flow and surfactant transport are formulated in Eqs. (3.2)-(3.7):

$$\nabla \cdot \tilde{\mathbf{u}} = 0, \quad \tilde{\rho} Re \left(\frac{\partial \tilde{\mathbf{u}}}{\partial \tilde{t}} + \tilde{\mathbf{u}} \cdot \nabla \tilde{\mathbf{u}} \right) = -\nabla \tilde{p} + \nabla \cdot \left[\tilde{\mu} (\nabla \tilde{\mathbf{u}} + \nabla \tilde{\mathbf{u}}^T) \right] + \frac{1}{Ca} \int_{\tilde{A}} \left(\tilde{\sigma} \tilde{\kappa} \mathbf{n} + \nabla_s \tilde{\sigma} \right) \delta \left(\tilde{\mathbf{x}} - \tilde{\mathbf{x}}_f \right) d\tilde{A}, \tag{3.2}$$

$$\tilde{\rho}\left(\mathbf{x}, t\right) = \frac{\rho_d}{\rho_c} + \left(1 - \frac{\rho_d}{\rho_c}\right) \mathcal{H}\left(\mathbf{x}, t\right), \quad \tilde{\mu}\left(\mathbf{x}, t\right) = \frac{\mu_d}{\mu_c} + \left(1 - \frac{\mu_c}{\mu_d}\right) \mathcal{H}\left(\mathbf{x}, t\right), \tag{3.3}$$

$$\frac{\partial \tilde{\Gamma}}{\partial \tilde{t}} + \nabla_s \cdot (\tilde{\Gamma} \tilde{\mathbf{u}}_t) = \frac{1}{Pe_s} \nabla_s^2 \tilde{\Gamma} + Bi \left(k \tilde{C}_s (1 - \tilde{\Gamma}) - \tilde{\Gamma} \right), \tag{3.4}$$

$$\frac{\partial \tilde{C}}{\partial \tilde{t}} + \tilde{\mathbf{u}} \cdot \nabla \tilde{C} = \frac{1}{Pe_c} \nabla \cdot (\nabla \tilde{C}), \tag{3.5}$$

$$\mathbf{n} \cdot \nabla \tilde{C}|_{interface} = -Pe_c Da Bi \left(k \tilde{C}_s (1 - \tilde{\Gamma}) - \tilde{\Gamma} \right), \tag{3.6}$$

$$\tilde{\sigma} = \max \left(\epsilon_\sigma, 1 + \beta_s \ln \left(1 - \tilde{\Gamma} \right) \right) \tag{3.7}$$

with ϵ_σ set to 0.05. The dimensionless numbers shown in the above equations are defined

by

$$Re = \frac{\rho_c U_{sc} l_c}{\mu_c};\ Ca = \frac{\mu_c U_{sc}}{\sigma_s};\ Pe_c = \frac{U_{sc} l_c}{D_c};\ Pe_s = \frac{U_{sc} l_c}{D_s};\ Bi = \frac{k_d l_c}{U_{sc}};$$
$$Da = \frac{\Gamma_\infty}{l_c CMC};\ k = \frac{k_a CMC}{k_d}, \tag{3.8}$$

where Ca and Re are the liquid capillary and Reynolds numbers, respectively; in which μ_c is the continuous phase viscosity; Pe_c and Pe_s are the bulk and interfacial Peclet numbers that represent the interplay between convective and diffusive forces for the surfactant species at the bulk and interface, respectively, in which D_c and D_s are the (constant) surfactant diffusion coefficients in the bulk continuous phase and the plane of the interface, respectively. The Biot number, Bi, represents the competition between the time-scales of desorption and convection, characterised by k_d^{-1} and l_c/U_{sc}, respectively. Finally, k represents the competition between adsorption and desorption time-scales, characterised by $(k_a CMC)^{-1}$ and k_d^{-1}, respectively. Lastly, the Damkohler number, Da, provides a dimensionless measure of interfacial saturation with surfactant.

The continuity and momentum equations (Eq. (3.2)) are written in a three-dimensional Cartesian domain using a single-fluid formulation. $\mathcal{H}\left(\tilde{\mathbf{x}}, \tilde{t}\right)$ represents a smoothed Heaviside function that takes the value of zero in the continuous phase and unity in the dispersed phase. The normal and tangential components of the interfacial tension force are expressed by the last two terms on the right-hand-side (RHS) of Eq. (3.2), respectively. The latter term representing the interfacial tension gradients across the interface, which give rise to Marangoni stresses; $\tilde{\kappa}$ corresponds to the interface curvature and $\delta(\tilde{\mathbf{x}} - \tilde{\mathbf{x}}_f)$ is the three-dimensional Dirac delta function equal to unity at the interface ($\tilde{\mathbf{x}} = \tilde{\mathbf{x}}_f$) and zero elsewhere. In Eq. (3.4), $\nabla_s = (\mathbf{I} - \mathbf{nn}) \cdot \nabla$ is the surface gradient operator, $\mathbf{n}$ is the outward-pointing unit normal to the interface, and $\mathbf{I}$ is the identity tensor; $\tilde{\mathbf{u}}_t = (\tilde{\mathbf{u}}_s \cdot \tilde{\mathbf{t}})\tilde{\mathbf{t}}$ corresponds to the tangential velocity, where $\tilde{\mathbf{u}}_s$ is the surface velocity, and $\mathbf{t}$ is the unit vector tangent to the interface. The last terms on the RHS of Eq. (3.4) and Eq. (3.7) represent the source term for surfactant exchange between the interface and the section of the bulk immediately adjacent to the interface.

As seen from figure 1(b) and Eq. (3.7), the dependence of σ on Γ is described by a non-linear Langmuir equation of state in which $\beta_s = \Re T \Gamma_\infty / \sigma_s$ modulates this dependency, as suggested by Muradoglu & Tryggvason (2014); $\Re$ and T are the ideal gas constant and the temperature, respectively. The components of the interfacial tension force that induce Marangoni stresses can be written in terms of Γ by

$$\frac{1}{Ca} \nabla_s \tilde{\sigma} \cdot \mathbf{t} \equiv \frac{\tilde{\tau}}{Ca} = -Ma \frac{1}{(1 - \tilde{\Gamma})} \nabla_s \tilde{\Gamma} \cdot \mathbf{t}, \tag{3.9}$$

where $\tilde{\tau}$ is the dimensionless Marangoni stress and $Ma \equiv \beta_s / Ca$ represents a Marangoni parameter.

From the properties of TX100 and the operating conditions of the system, the relevant dimensionless numbers that characterise the system are given by $Re = 2.35$, $Ca = 4.33 \times 10^{-3}$, $Pe_c = Pe_d = 2.35 \times 10^5$, $Bi = 8.41 \times 10^{-5}$, $Da = 1.04 \times 10^{-3}$, $k = 5.55 \times 10^3$, $\beta_s = 0.10$, and $Ma = 23.08$. We define a capillary time-scale as $\tau_{cap} = \sqrt{\rho_c l_c^3 / \sigma_s} = 1.31 \times 10^{-3}$ s, a velocity time-scale as $\tau_{vel} = \sqrt{\sigma_s / (\rho_c l_c)} = 2.99 \times 10^{-1}$ s, and a Marangoni time-scale as $\tau_{mar} = \mu_c l_c / \Delta\sigma = 6.16 \times 10^{-5}$ s. Here, it has been assumed that $D_c = D_s = \mathcal{D}$, and Γ_∞ and $K_L = k/CMC$ were found by fitting the experimental data in figure 1(b) to the Langmuir–Szyszkowski equation (Teipel & Aksel 2001), as in previous work (Kalli *et al.* 2022). Γ was calculated using the Langmuir equation of state with the measured experimental values of σ for each $\tilde{C}$ (see Eq.(3.7) and plotted in a dimensionless form

TABLE 1. Physical Properties of TX100 surfactant.

Physical properties		TX100
Γ_∞	(mol/m^2)	1.42×10^{-6}
K_L	(m^3/mol)	1585.00
k_d	(1/s)	0.0065
k_a	(m^3/mol s)	10.3
$\mathcal{D}$	(m^2/s)	5×10^{-11}

on the secondary axis of figure 1(b)). Using the literature value of TX100 desorption in water (k_d) (Gassin *et al.* 2012), k_a was calculated using $k_\mathrm{a} = K_L k_\mathrm{d}$ and shown in Table 1. Finally, the diffusion coefficient, $\mathcal{D}$, was estimated using the Wilke-Chang correlation (Wilke & Chang 1955).

Fully three-dimensional direct numerical simulations were performed within the context of the Level Contour Reconstruction Method (LCRM) for the interface advection, as previously detailed in Shin & Juric (2002) and Shin *et al.* (2005, 2017, 2018). This method handles the interface and the forces arising from surface tension through a hybrid front-tracking/level-set technique in conjunction with surfactant transport at the interface and bulk. At the inlet branches, an analytical solution following a Poiseuille profile is set for the velocity, together with a Neumann condition for the pressure ($\partial p/\partial \mathbf{n} = 0$). The full derivation of this velocity profile (Eq.(3.10) in dimensionless form) in the cross-section shown in figure 1(c) (right) can be found in §A. At the outlet, a Neumann condition is specified for both velocity and pressure. The walls are treated as no-slip boundaries. For the surfactant-laden cases, Neumann conditions are set for surfactant concentration on all boundaries, with the exception of the disperse phase inlet. For this inlet, C is specified as a constant value according to the experimental setup ($\tilde{C} = 0.06$ and $\tilde{C} = 0.21$), and Γ as calculated in figure 1(b).

$$\tilde{\mathbf{u}}(\tilde{x},\tilde{y}) = \begin{cases} \tilde{\mathcal{A}}\left(\dfrac{(\tilde{y}-\tilde{y_0})^2}{\tilde{R}^2} - 1\right) & \text{if } |\tilde{x}-\tilde{x_0}| \leqslant \tilde{L} \\ \tilde{\mathcal{A}}\left(\dfrac{(\tilde{x}-\tilde{x_0}-\tilde{L})^2}{\tilde{R}^2} + \dfrac{(\tilde{y}-\tilde{y_0})^2}{\tilde{R}^2} - 1\right) & \text{otherwise,} \end{cases} \tag{3.10}$$

where $\mathcal{A} = \frac{-Q}{\frac{8}{3}RL + \frac{\pi}{2}R^2}$, Q represents the flow rate of the phase on each inlet (continuous for the two lateral branches and disperse for the central branch), x_0 and y_0 are the coordinates of the centre points of the inlet cross sections, and $R = w_c/2$ and $L = (l_c - w_c)/2$, as highlighted in figure 1(c). Each variable has been non-dimensionalised according to the scaling parameters described previously, with $\tilde{\mathcal{A}} = \frac{-\tilde{Q}U_{sc}}{\frac{8}{3}\tilde{R}\tilde{L} + \frac{\pi}{2}\tilde{R}^2}$.

3.2. *Validation*

The numerical simulation in an identical geometry was validated experimentally with a surfactant-free system in previous work (Kahouadji *et al.* 2018). Further validation with experimental results for surfactant-laden cases is made in this section. As seen in previous work (Kalli et al., 2022), a semi-empirical model can be developed to relate the dimensionless drop diameter to the Capillary number and thus the interfacial tension, with the latter being proportional to the drop size in a microfluidic system. As a result,

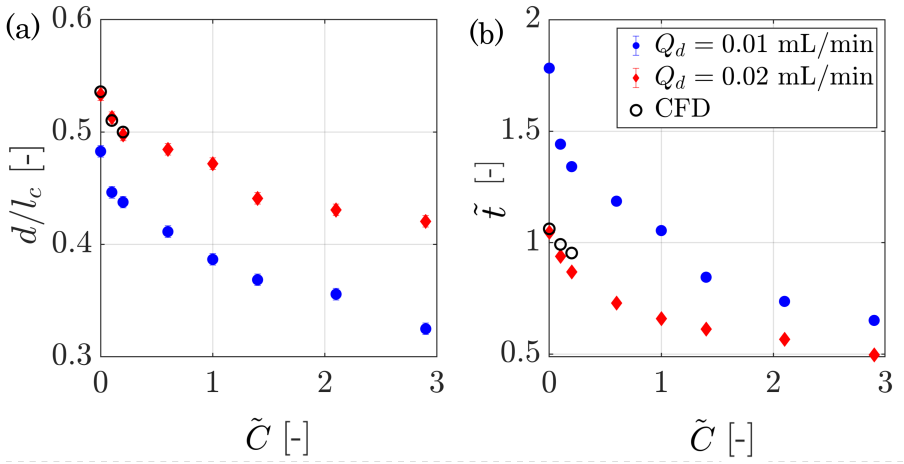

FIGURE 3. Effect of TX100 concentration on dimensionless drop (a) diameter (d/l_c) and (b) formation time ($\tilde{t}$)).

the addition of surfactant is expected to result in smaller drops with shorter formation times, due to the lower interfacial tension.

Figure 3(a) shows the effect of surfactant addition on the drop diameter for Q_c = 0.12 mL/min and 0.01 mL/min $\leqslant Q_d \leqslant$ 0.02 mL/min. As $\tilde{C}$ increases from 0 to 3, the dimensionless drop diameter d/l_c decreases for both flowrates, due to the lower interfacial tension. Larger drops are observed at higher Q_d as expected.

The effect of surfactant addition on the drop formation time for Q_c = 0.12 mL/min and 0.01 mL/min $\leqslant Q_d \leqslant$ 0.02 mL/min is shown in figure 3(b). As $\tilde{C}$ increases from 0 to 8.6, the dimensionless formation time $\tilde{t}$ decreases for both flowrates, due to lower interfacial tension. Shorter formation times are observed at larger Q_d, as opposed to drop diameter. The above results are compared with the numerical simulations and good agreement is found, with an average error of 0.5% for d/l_c and 8.6% for $\tilde{t}$. The error between the high-speed imaging (HSI) and the μPIV experiments was below 1%.

4. Results and discussion

The vortical structures and the velocity fields obtained from the CFD simulations and the high-speed μPIV experiments in surfactant-free and surfactant-laden systems, as well as the concentration profiles in the bulk and at the interface are discussed here, for all stages of the drop formation process. The results for the surfactant-free case will be discussed first to show the spatio-temporal evolution of the interface, as well as the vortical structures during each stage. In addition the surfactant concentrations in the bulk and at the interface for the various stages of drop formation will be discussed based on the CFD simulations.

4.1. *Surfactant-free case*

The spatio-temporal evolution of the interface during the complete drop formation process was first simulated for the surfactant-free case. Figure 4 shows the changes in the shape of the interface during expansion (a), necking (b), and pinch-off (c) for Q_d = 0.02 mL/min and Q_c = 0.12 mL/min. A different output time-step is used for each stage equal to 1 ms, 0.5 ms, and 0.1 ms, respectively, with the longest one used for the expansion stage

and the shortest for pinch-off. Specifically, the evolution of the interface is slow during expansion, becomes moderately rapid during necking, and very rapid just before pinch-off. In previous work, expansion times were also found to be longer compared to necking ones, for both surfactant-free and surfactant-laden cases in the dripping regime (Kalli & Angeli 2022). A similar trend was seen by Kahouadji *et al.* (2018) for pancake-shaped drops.

The vortical structures inside the drop are shown in figure 4(d) for the expansion and necking stages and in figure 4(e) for pinch-off. The velocity fields from the experiments with and without surfactant are shown in figure 5, which agree very well with the simulation results. Initially for the surfactant-free case (at $\tilde{C} = 0$ and $\tilde{t} = 0.10$, figure 4d), two vortical structures are seen close to the front of the drop which grow larger and move closer to the interface later on (at $\tilde{t} = 0.50$). This is in agreement with the experimental results, where large internal circulation patterns are observed in expansion at $\tilde{t} = 0.10$ and $\tilde{t} = 0.50$ (figures 5a-b respectively). The circulation pattern is more pronounced in the second stage of expansion ($\tilde{t} = 0.50$, figure 5b), where two circulation zones are clearly seen, one on each side of the growing drop and high velocities in the middle, reaching a maximum of $|U_{max}|/U_{sc} = 0.45$. From the shape of the interface (black dotted line) it is clear that originally the drop grows in the radial direction, as the continuous phase obstructs the flow of the dispersed phase. The high velocities on the sides of the dispersed phase during expansion suggest that the liquid is mainly transported through the sides of the drop. This is in agreement with observations reported previously by several authors (Pirbodaghi *et al.* 2015; Roumpea *et al.* 2019). Previous works using Ghost Particle Velocimetry in rectangular flow-focusing microchannels reported a stagnation point at the base of the growing drop, during the second stage of expansion, but no significant circulation in the surfactant-free case. Even though a stagnation point can be seen in this work during the second stage of expansion (Figure 5b), the presence of the strong circulation in this study can be attributed to the differences in microchannel geometries (oval in the present study and rectangular in the study of Kiratzis *et al.* (2022)) and higher flowrates used. The predominant reason for this difference is due to the presence of corner flow in the gutters of the rectangular channel, which is absent in this work with an oval flow-focusing geometry. This can also reverse the direction of the flow fields after the drop has formed (Kovalchuk & Simmons 2021; Mießner *et al.* 2020).

As the drop grows, it obstructs the inlet of the oil phase, which now pushes the interface perpendicular to the drop and changes its curvature. This marks the beginning of the necking stage, with the neck defined as the bridge between the growing drop and the dispersed phase remaining attached to the inlet. The curvature of the interface becomes negative and the pressure build-up from the continuous phase causes the flow to be higher in the neck compared to the rest of the dispersed phase (with $|U_{max}|/U_{sc} = 0.25$), while the velocities near the interface decrease. In addition, the vortical structures decrease in size ($\tilde{t} = 0.67$ in figures 4d and 5c). This indicates that the transport of the dispersed phase from the sides is significantly weaker than in the expansion stage. As the process approaches pinch-off (see figure 4e, left panel), large vortical structures form in the region of the dispersed phase that remains attached to the inlet. Immediately after the pinch-off, the vortical structures grow large in the middle of the cross-junction (figure 4e, right panel). This vortex dipole just before and at pinch-off was also observed during the formation of surfactant-free plugs (Kahouadji *et al.* 2018). Another agreement between the two works is the stagnation point present just at the location of pinch-off. A small satellite drop is also seen at the point where the neck broke. The distance between four subsequent drops is equal, as shown in figure 4(f), indicating that the drop formation process is periodic with exactly the same formation time of 13.5 ms in each cycle.

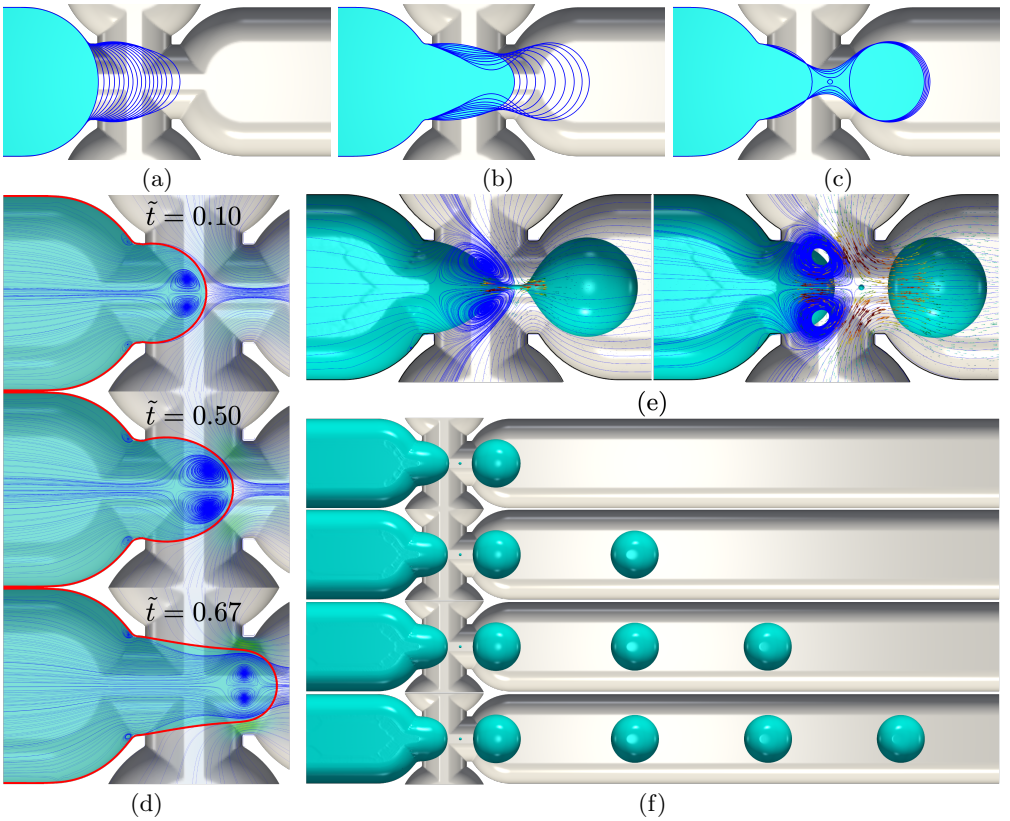

FIGURE 4. Numerical results for the surfactant-free case generated with $Q_d = 0.02$ mL/min and $Q_c = 0.12$ mL/min. Panels (a)-(c) depict the spatio-temporal evolution of the interface with a time difference between the curves is 1 ms, 0.5 ms, and 0.1 ms, respectively; (d) highlights the vortical structures for three different times that can also be compared with experimental PIV of figures 5(a,b,c) (shown in red lines); (e) shows the development of a neck followed by pinch-off which is accompanied by satellite formation; (f) shows top-views of the periodic drop formation in the channel with a period of 13.5 ms.

4.2. *Surfactant-laden cases*

4.2.1. *Expansion and necking stages*

Upon addition of the TX100 surfactant at $\tilde{C} = 0.06$, the velocity fields change significantly from their surfactant-free counterparts throughout all stages of the drop formation process. At the start (see figure 5d at $\tilde{t} = 0.08$), the average velocities appear higher and more uniform at the back of the forming drop and a less intense circulation pattern can be seen in the centre. The two circulation zones still appear in the second phase of the expansion stage (see figure 5e at $\tilde{t} = 0.33$), however, their velocities are lower than in the surfactant-free case. During the necking stage at TX100 concentrations below CMC (figure 5f), higher velocities are observed near the neck, with maximum values of $|U_{max}|/U_{sc} = 0.45$. The reduced interfacial tension due to the presence of surfactant accelerates the neck thinning and results in high velocities (figure 5f at $\tilde{t} = 0.41$), as also observed by Kiratzis *et al.* (2022). The circulation pattern completely disappears during necking at low TX100 concentrations, which agreed with the CFD simulations. For concentrations above the CMC, during the first expansion phase (see figure 5g at $\tilde{t} = 0.05$), velocities are high inside the whole of the growing drop, reaching a maximum

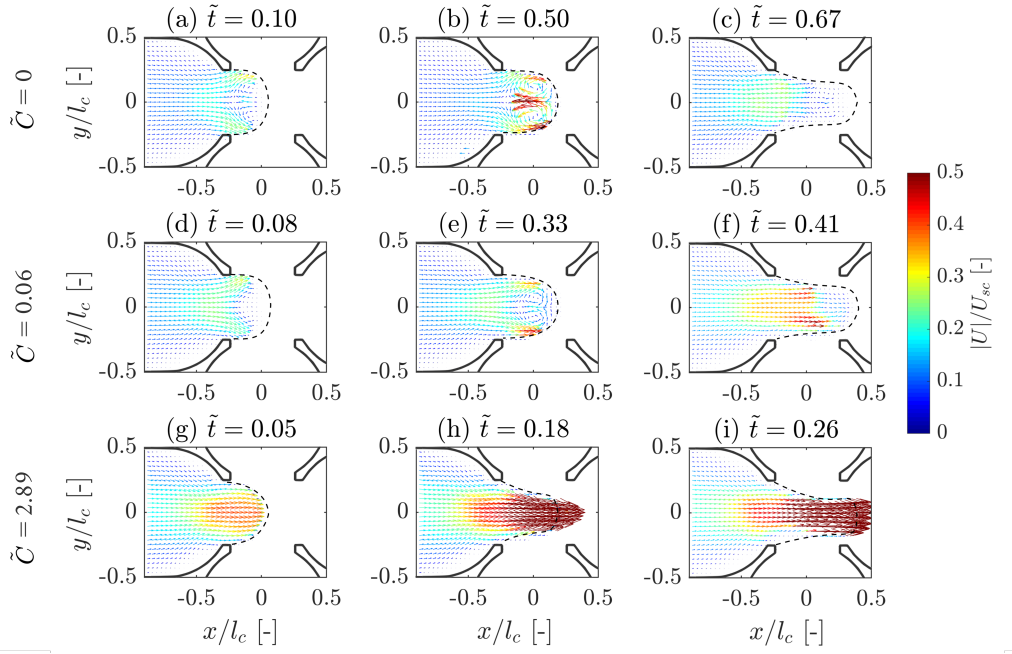

FIGURE 5. Effect of TX100 concentration on velocity fields from PIV measurements during expansion and necking stages at $Q_d = 0.02$ mL/min for (a) – (c) $\tilde{C} = 0$, (d) – (f) $\tilde{C} = 0.06$ and (g) – (i) $\tilde{C} = 2.89$.

of $|U_{max}|/U_{SC} = 0.4$. Velocities then increase significantly as shown in figures 5(h)-(i) as the drop expands into the main channel, and at the necking stage at $\tilde{t} = 0.18$ and 0.26, reaching a $|U_{max}|/U_{sc} = 0.5$ (More details are discussed in subsection 4.2.3).

As discussed by several authors, high dispersed phase flowrates can enhance surfactant mass transfer possibly due to increased convection, especially in the TX100 case which is convective mass transfer controlled at low concentrations (Wang *et al.* 2009, 2016). In this work, high velocities near the sides of the forming drops are observed at $Q_d = 0.02$ mL/min in both the simulations and experiments, which can enhance surfactant mass transport to the interface, as opposed to $Q_d = 0.01$ mL/min. This could explain the lower dynamic interfacial tension measured at $Q_d = 0.02$ mL/min compared to the one in $Q_d = 0.01$ mL/min in our previous work (Kalli *et al.* 2022), even though drops formed faster and surfactant had less time to transfer to the interface (see figure 3b).

4.2.2. *Pinch-off*

Pinch-off is further discussed in this section, using both the numerical and experimental results. The effect of TX100 surfactant on drop shape and velocity fields at pinch-off from HSI and μPIV experiments, as well as CFD simulations at $Q_d = 0.02$ mL/min as shown in figure 6. As can be seen in figures 6(a), (d) and (g), smaller droplets are formed upon TX100 addition and satellite drops are seen after pinch-off. It should be noted that the shadow from the edge of the channel observed when using HSI does not exist in the μPIV images, which can mislead the comparison of the droplet sizes in figures 6(c and f). In the case of no surfactant present, high velocities at the rear of the formed drop and circulation patterns in the dispersed phase remaining attached to inlet are seen in figure 6(b-c) (see also figure 4). The higher velocities at the rear of the drop as opposed to its front are also observed in the surfactant-free simulations of Zhao *et al.* (2015). Similar

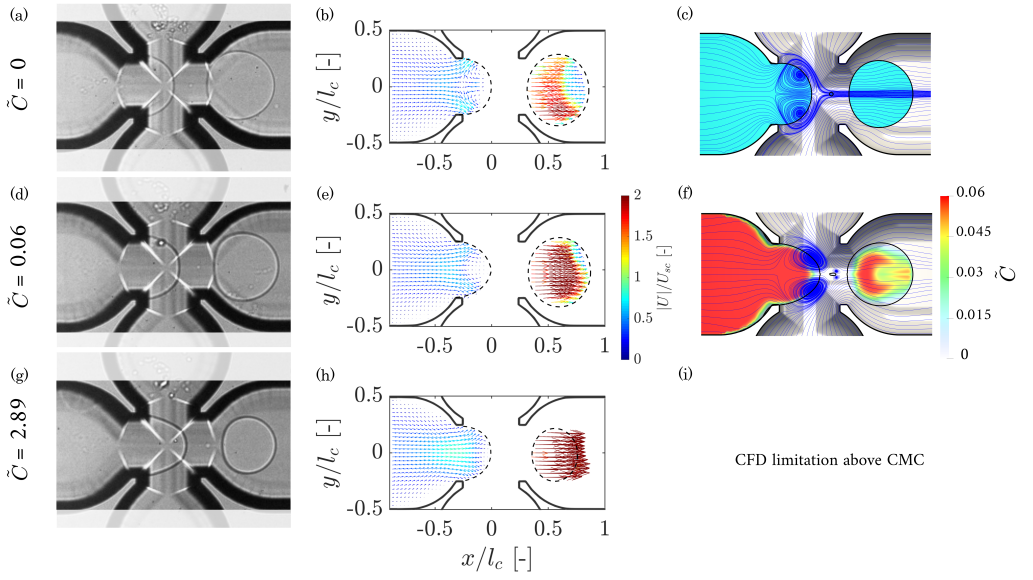

FIGURE 6. Effect of TX100 concentration on velocity fields from HSI experiments (a), (d) and (g), PIV measurements (b), (e) and (h) and CFD (c), (f) and (i) at the pinch-off point for 0.02 mL/min for (a) – (c) $\tilde{C} = 0$, (d) – (f) $\tilde{C} = 0.06$ and (g) – (i) $\tilde{C} = 2.89$.

observations were reported from CFD simulations of mass transfer in a flow-focusing microchannel by Lan *et al.* (2014).

When surfactant is added at concentrations below CMC, smaller droplets form due to the lower interfacial tension and a weaker circulation pattern is seen at the remaining dispersed phase. The velocities inside the formed droplet are higher compared to the surfactant-free case (figure 6e-f at $\tilde{C} = 0.06$). A stagnation point is also observed in the CFD output just at pinch-off for both surfactant-free and surfactant-laden cases. At concentrations above the CMC, the experimental μPIV results show that the circulation pattern completely disappears and uniform velocity fields are observed in the formed droplet, with $|U_{max}|/U_{sc} = 0.5$ (figure 6h at $\tilde{C} = 2.89$). As was discussed above, the model does not account for micelle formation, and no numerical results are shown for concentrations above CMC.

4.2.3. *Concentration distribution*

Figure 7 shows the relative bulk concentration of the TX100 surfactant (a), $\tilde{C}$, the vortical structures (b), and the interfacial concentration (c), ($\tilde{\Gamma}$), during the drop formation process at concentrations below CMC ($\tilde{C} = 0.06$). The concentration profile of the surfactant in the bulk follows the circulation patterns as seen in the expansion stage ($\tilde{t} = 0.39$, top of figures 7a-b). During the necking stage, the circulation is weaker and the surfactant transfers downstream, following the drop growth and into the main channel ($\tilde{t} = 0.78$). Just before pinch-off, the two circulation zones in the drop disappear and the concentration of surfactant is high at the rear of the drop ($\tilde{t} = 0.98$). Large circulation patterns appear at the front of the phase remaining attached to the inlet, which grow larger after drop detachment ($\tilde{t} = 0.99$). Interestingly, the small satellite drop appears to have no surfactant. As also observed in the μPIV experiments, the circulation zones in all stages are smaller compared to the surfactant-free case. This is possibly due to

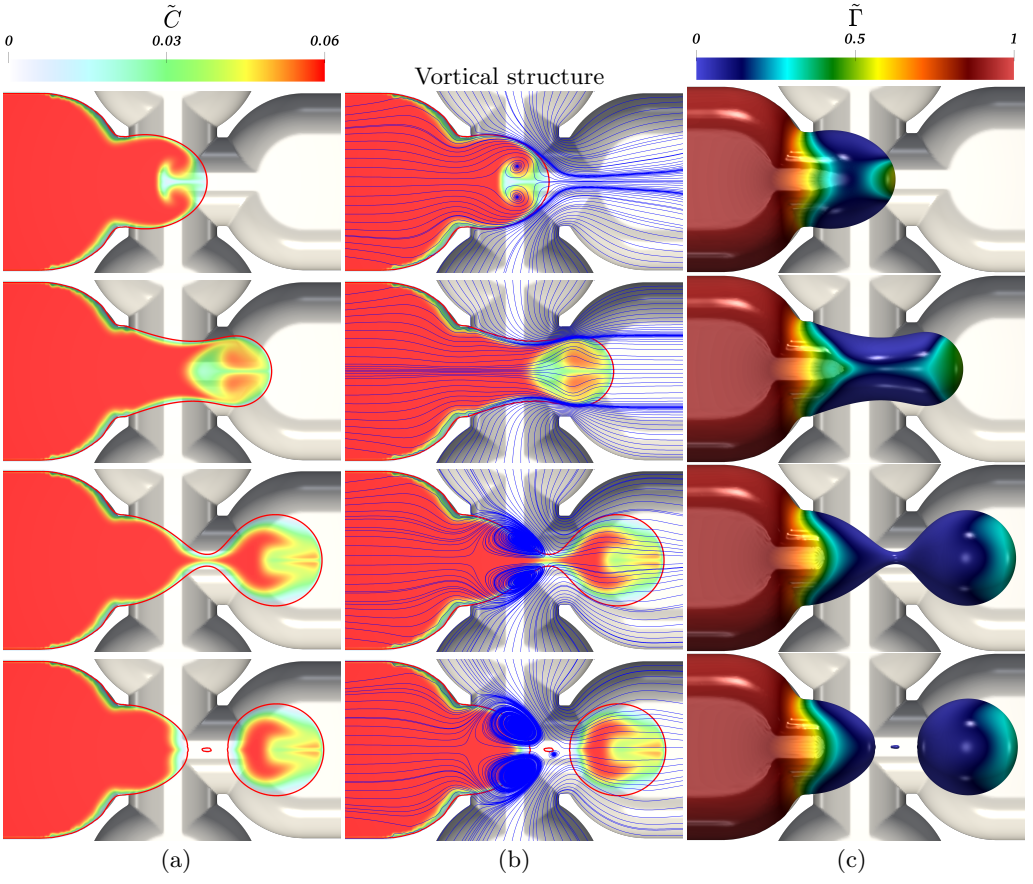

FIGURE 7. Spatio-temporal evolution of (a) the relative bulk surfactant concentration $\tilde{C}$, (b) the vortical structures in the channel reference frame and (c) the relative interfacial surfactant concentration $\tilde{\Gamma}$, respectively. The snapshots from top to bottom correspond to times $\tilde{t} = 0.39$, 0.78, 0.98, and 0.99, respectively, and $\tilde{C} = 0.06$.

Marangoni forces acting in the opposite direction to the circulation when surfactant is present.

As previously discussed, information on the surfactant concentration at the interface is paramount in understanding the effect of TX100 on the drop formation process. The spatio-temporal evolution of the relative interfacial concentration ($\tilde{\Gamma}$) is shown in figure 7(c). As can be seen the interfacial concentration of the surfactant is high (and equal to the equilibrium value) at the left part of the channel, and before the cross-junction where the interface forms. At the interface initially there is very little surfactant concentration, apart from the tip of the drop. Even at the tip, however, the concentration is below the equilibrium value. This concentration profile remains at all stages of the formation process, including expansion (top), necking (middle) and pinch-off (bottom). The difference in surfactant concentration along the interface will cause Marangoni stresses that can affect the drop formation time and the velocity fields inside the drop; this will be discussed further in §4.2.4.

4.2.4. *Marangoni stresses*

Marangoni stresses are usually discussed in works for drop-coalescence (Constante-Amores *et al.* 2021; Dong *et al.* 2019), rising bubbles (Bastani *et al.* 2018), liquid bridges (Kovalchuk *et al.* 2017; Kamat *et al.* 2018) and jet formation (Antonopoulou *et al.* 2021), but less frequently during the fast process of drop formation. In this section, Marangoni stresses at the interface will be calculated and presented as a function of time and space for the first time during the whole drop formation process. Additionally, the competition between Marangoni stresses and the interfacial tension reduction caused by the surfactant absorption will be explored in all dimensions of the forming drop.

Figure 8 shows the shape of the interface and the dimensionless interfacial concentration of surfactant during drop formation, with the magnitude of $\tilde{\Gamma}$ shown in colour in (a) and (b) for top- (x-y plane) and side- (x-z plane) views, respectively. The corresponding local interfacial tension (σ/σ_s) and the Marangoni stress ($\nabla(\sigma/\sigma_s)\cdot\mathbf{t}$) are shown in figures 8(c-d) and (e-f), respectively. The 3 profiles represent the expansion stage at $\tilde{t} = 0.39$, the initial part of the necking stage at $\tilde{t} = 0.78$ and the final part of necking before pinch-off at $\tilde{t} = 0.98$, for $Q_d = 0.02$ mL/min and $Q_c = 0.12$ mL/min. The concentration gradient at the interface decreases as the drop grows, with the concentration at the drop tip reaching a maximum of $\tilde{\Gamma} = 0.58$ at $\tilde{t} = 0.39$, which decreases to $\tilde{\Gamma} = 0.48$ at $\tilde{t} = 0.78$ and $\tilde{\Gamma} = 0.35$ at $\tilde{t} = 0.98$ (as also seen in figure 7(c)). This causes a weaker interfacial tension gradient for the top-view as observed from the slope in figure 8(c) which decreases as the drop forms. The Marangoni stresses on the interface are small and in the opposite direction to the flow, as seen from the negative peaks in figure 8(e) with $\nabla(\sigma/\sigma_s)$ = -2.4, -0.7 and -0.3 at $\tilde{t} = 0.39, 0.78$ and 0.98 respectively ($0.4 < x/l_c < 1.2$). The positive peak in the direction of the forming drop, around $x/l_c = 0$ in the range of $0.0 < x/l_c < 0.2$ with $\nabla(\sigma/\sigma_s)\cdot\mathbf{t} \sim 1.5$ exists for all three stages, but is far from the neck region to contribute to pinch-off.

The flow of the continuous phase from both the top and bottom inlets ($Q_c = 0.12$ mL/min) is high enough to sweep surfactant molecules away from the neck towards both sides of the neck and results in an essentially surfactant-free interface at the neck region. The depletion of surfactant in the neck area between $0.2 < x/l_c < 0.9$ (as also seen in figure 7c) and the flat concentration profile of $\tilde{\Gamma}$ show that there are no Marangoni stresses to affect the process of pinch-off. The shorter drop formation times observed when surfactants are present are caused by the lower interfacial tension compared to the surfactant-free case. The effect of this dominates over Marangoni stresses as the high continuous flowrates cleans the interface during the whole formation process (see Figure 8. The maximum in $\tilde{\Gamma}$ at all times close to the drop tip causes local Marangoni stresses in that area whose strength decreases with time. These stresses slow down the velocity inside the drop and weaken the circulation intensity (as discussed in §4.2) rather than delay pinch-off. This is opposite to the case of jet formation where Marangoni stresses delay break-up and result in longer times to pinch-off (Kalli & Angeli 2022).

The influence of the continuous phase flowrate on the surfactant distribution at the interface is obvious when the top- and side-views are compared. The surfactant concentration distribution at the interface is less uniform in the side- than in the top-view, while the neck area has some surfactant, apart from the last part of the necking stage (Figure 8b). This results in a lower interfacial tension overall, which will contribute to the decrease in drop formation time. Marangoni stresses now appear with peaks close to the neck region between $0.1 < x/l_c < 0.3$ at $\tilde{t} = 0.78$ and $0.1 < x/l_c < 0.2$ at $\tilde{t} = 0.98$. Nonetheless their magnitude is small ($\nabla(\sigma/\sigma_s)\cdot\mathbf{t} < \mathbf{1}$) and are not close to the thinning part of the neck ($0.4 < x/l_c < 0.6$ at $\tilde{t} = 0.98$) so should not to contribute to pinch-off.

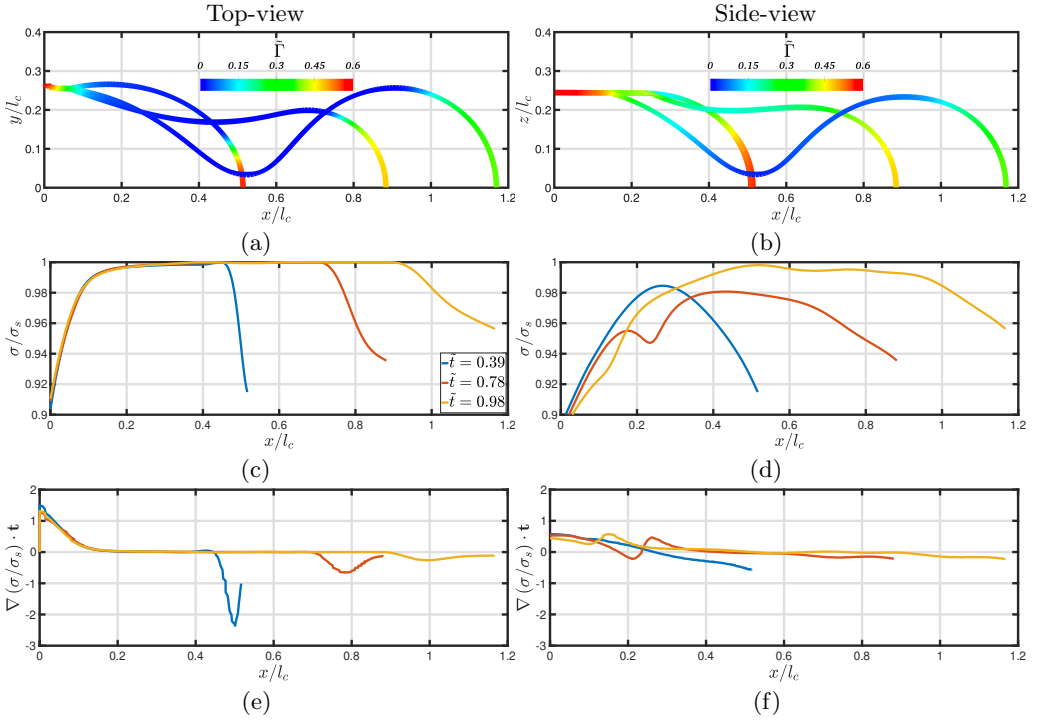

FIGURE 8. Quantitative measures highlighting (a)-(b) the interface shape and the interfacial surfactant distribution with the magnitude of Γ/Γ_∞ shown in colour, (c)-(d) the corresponding local interfacial tension σ/σ_s, and (e)-(f) the Marangoni stress $\nabla(\sigma/\sigma_s)\cdot\mathbf{t}$, for top- and side-views, respectively.

Antonopoulou *et al.* (2021) compared experimental results with numerical simulations of a weak ($\beta_s = 0.1$, low CMC, identical to this study) and a strong ($\beta_s = 1$, high CMC) surfactant during jet formation and break-up. It was found that the distribution of the weak surfactant at the interface was less uniform as opposed to the strong surfactant. Even though surfactant accumulation near the neck follows the opposite trend between the formation of drops (low Γ at drop pinch-off) and jets (high Γ at jet break-up), there is agreement on the fact that surfactant concentration gradients and thus Marangoni stresses decrease with time during the formation process, as seen in this work.

4.3. *Fully formed drops*

In order to investigate surfactant transport in the whole drop volume, the vortical structures and surfactant concentrations of the formed drops as obtained by the CFD simulations are shown in figure 9 for surfactant-laden (c-d) cases after pinch-off (at the end of the channel, $10 \times d$). The vortical structures for surfactant-free drops are shown in figures 8 (a-b) for comparison. The difference in the shape of the formed drop for top- (a),(c) and side-(b),(d) views is due to the channel dimensions, as explained in §2 and §3. In the surfactant-free case, the vortical structures are completely symmetrical from the top-view, while a strong vortex dipole is seen from the side-view near the rear boundaries of the drop. The opposite is seen in the surfactant-laden drop; a strong vortex dipole is forming in the centre of the top-view, while no circulation is seen in the side-view.

Both bulk and interfacial concentrations of the formed drops are plotted in figure 9, in their dimensionless form as $\tilde{C}$ and $\tilde{\Gamma}$, respectively. For $\tilde{C}$, the surfactant concentration is high in the centre and low around the periphery of the drop in both the top- and

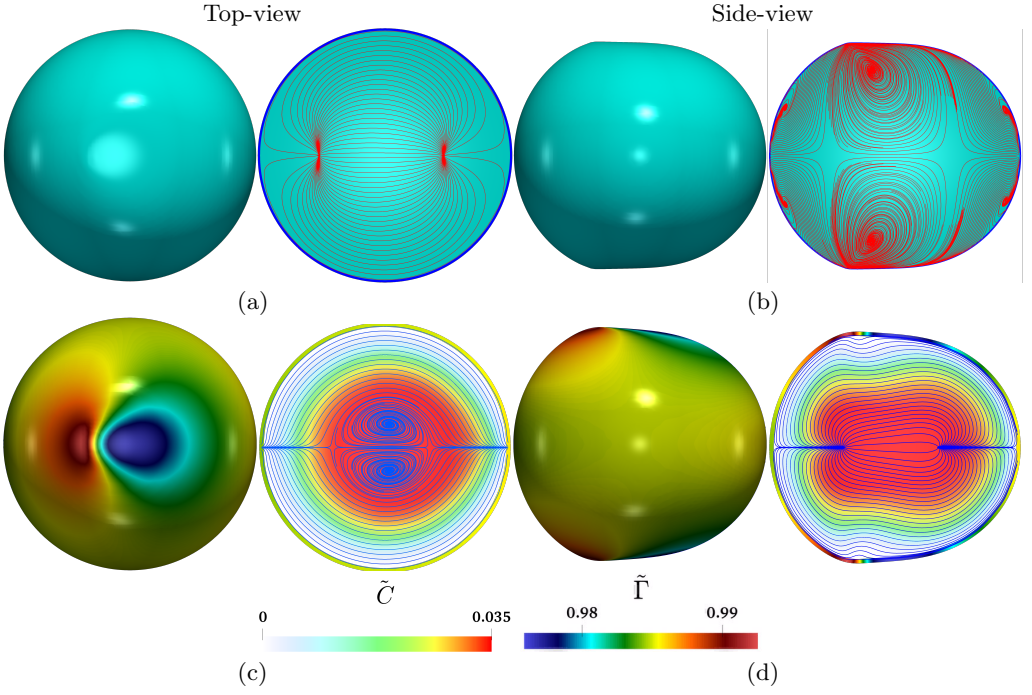

FIGURE 9. Top- and side-views of resulting drop for the surfactant-free case (a-b) and surfactant-laden case (c-d) accompanied with their vortical structures in the moving reference frame. Both cases are for $Q_d = 0.02$ mL/min, $Q_c = 0.12$ mL/min and $\tilde{C} = 0.06$. These conditions correspond to the non-dimensional parameters: $Re = 2.35$, $Ca = 4.33 \times 10^{-3}$, $Pe_c = Pe_d = 2.35 \times 10^5$, $Bi = 8.41 \times 10^{-5}$ and $k = 5.55 \times 10^3$.

side-views. The variations in $\tilde{\Gamma}$ are small, as can be seen from the range of the scale in the figure. Here it should be noted that adsorption is significantly faster than desorption, as also expected from the large $K_L = 1585.00$ m^3/mol value. As mentioned in §3, $Bi = 8.41 \times 10^{-5}$ is very small, which can be considered negligible when compared to $k = 5.55 \times 10^3$, denoting negligible desorption as opposed to adsorption of surfactant at the interface. When compared to the concentrations during drop formation, it is obvious that the surfactant absorbs very fast after pinch-off. As seen in figure 7, the bulk concentration reaches the maximum value inside the drop throughout all stages ($\tilde{C} = 0.06$) and the interface is not saturated ($\tilde{\Gamma} < 1$). This is not the case for fully formed drops, where the bulk concentration is lower than the maximum value. However, there are some differences in the interfacial concentration of the surfactant. From the top-view, $\tilde{\Gamma}$ is seen to be higher at the rear of the drop. On the other hand, the interfacial concentration of the surfactant is larger near the rear edges of the drop from side-view. This is due to advection of surfactant at the back of the drop as it travels through the channel.

5. Conclusions

This paper presents a thorough study of the formation process of surfactant-laden drops inside a flow-focusing microchannel. High-speed imaging experiments (HSI) and novel micro-Particle Image Velocimetry (μPIV) experiments were used in conjunction with numerical CFD simulations, to obtain velocity and surfactant concentration profiles and understand the effects of surfactants on the different stages of the drop formation process. Surfactant concentrations below and above the critical micelle concentration (CMC)

were considered. The numerical simulation utilised a three-dimensional multiphase solver which accounted for the transport of soluble surfactants in the bulk and at the interface and was adapted to the context of the hybrid Front-Tracking/Level-set method.

A low viscosity silicone oil (4.6 mPa s) was used as the continuous phase and a mixture of 48% w/w water and 52% w/w glycerol was the dispersed phase. A non-ionic surfactant ($\mathrm{CMC}_{TX100} = 3.5\mathrm{mM}$) was added in the aqueous phase, at several concentrations below and above CMC. Numerical simulations for the drop formation in the microfluidic channel showed good agreement with experiments on drop size, formation time and vortical structures during drop formation.

Results revealed smaller dimensionless drop size (d/l_c) and shorter formation times ($\tilde{t}$) at higher surfactant concentrations ($\tilde{C}$) in the drop bulk due to the lower interfacial tension forces. During the drop expansion and necking stages, velocities at the back of the forming drop were higher at higher $\tilde{C}$ values while the circulation patterns completely disappeared at concentrations above the CMC. At the pinch-off point, the velocities were higher at the rear of the drop as opposed to the front, while circulation patterns in the dispersed phase remaining attached to the inlet were weaker when surfactant was added compared to the cases with no surfactant. The effect of the dispersed phase flowrate was also investigated and it was found that an increase in flowrate increased circulation intensity in the drop during the expansion stage and thus enhanced surfactant mass transport to the interface.

The surfactant concentrations in the bulk and at the interface of the formed drop were also explored. Marangoni stresses at the drop interface were calculated for all stages of drop formation and found to progressively weaken with formation time. It was concluded that the high continuous phase flowrate plays an important role in sweeping surfactants away from the neck region and contributed towards pinch-off mainly. The Marangoni stresses did not seem to affect the neck pinch-off but contribute mainly to the velocity profile inside the drop, as opposed to what is seen in jet formation and break-up.

In future work, a new experimental setup will be developed using μLIF techniques to trace both time and spatial evolutions of the surfactant concentration at the interface and compare with numerical results. Additionally, the numerical simulations will be expanded to model concentrations above CMC by accounting for micelle formation.

Acknowledgements. This work is supported by the Engineering and Physical Sciences Research Council, United Kingdom, through the EPSRC MEMPHIS (EP/K003976/1) and PREMIERE (EP/T000414/1) Programme Grants. M.K. would like to acknowledge the EPSRC Doctoral Training Programme (EP/ R513143/1) for her studentship. O.K.M. acknowledges funding from PETRONAS and the Royal Academy of Engineering for a Research Chair in Multiphase Fluid Dynamics. P.P. and L.K. acknowledge HPC facilities provided by the Research Computing Service (RCS) of Imperial College London for the computing time. D.J. and J.C. acknowledge support through HPC/AI computing time at the Institut du Developpement et des Ressources en Informatique Scientifique (IDRIS) of the Centre National de la Recherche Scientifique (CNRS), coordinated by GENCI (Grand Equipement National de Calcul Intensif) Grant 2022 A0122B06721. The numerical simulations were performed with code BLUE (Shin *et al.* (2017, 2018)) and the visualisations have been generated using ParaView.

We confirm that there is no conflict of interest.

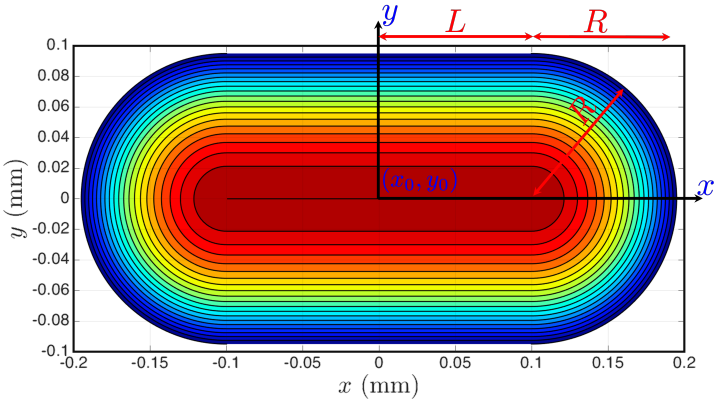

FIGURE 10. Normalised inlet velocity profile. The contours are equally spaced with steps of 0.05 and $(x_0, y_0) = (0, 0)$.

Appendix A. Inlet velocity profile

The cross-section of the three inlets is comprised of two main areas: two semi-circles of radius $R = w_c/2$ and a rectangular portion of dimensions $w_c \times (l_c - w_c)$. The coordinates of centre point of the cross-section are defined as x_0 and y_0, and the distance in the x-axis from the edge of the rectangular portion to the centre line as $L = (l_c - w_c)/2$. We begin with a general parabolic function consistent with a Poiseuille profile for the velocity at the rectangular portion ($f_1(x, y)$):

$$f_1(x, y) = a_1(x - x_0)^2 + b_1(y - y_0)^2 + c_1 \;\text{ if } (x - x_0) \in [-L, L], \tag{A 1}$$

where a_1, b_1 and c_1 are constants. Applying a no-slip condition at the channel walls ($f_1(x, \pm R) = 0$) and considering symmetry across the x-axis, we obtain $a_1 = 0$ and $b_1 = -c_1/R^2$:

$$f_1(x, y) = -\frac{c_1}{R^2}(y - y_0)^2 + c_1, \tag{A 2}$$

We define the parabolic profile for the circular sections in cylindrical coordinates ($f_2(r, \theta)$):

$$f_2(r, \theta) = a_2(L + \sin\theta)^2 + b_2(r\cos\theta)^2 + c_2 \;\text{ if } (x - x_0) \leqslant -L \;\text{ or } (x - x_0) \geqslant L, \tag{A 3}$$

where $x - x_0 = L + \sin\theta$ and $y - y_0 = r\cos\theta$. Applying a continuity condition at the limit between the rectangular and circular sections, $\frac{\partial f_1}{\partial y}\Big|_{x-x_0=L} = \frac{\partial f_2}{\partial r}\Big|_{\theta=0,\pi}$, as well as the no-slip condition at the walls, $f_2(\theta, R) = 0$, we obtain $b_2 = b_1 = -c_1/R^2$ and $c_1 = c_2$

$$f_2(r, \theta) = -\frac{-c_1}{R^2}(\sin\theta)^2 - \frac{c_1}{R^2}(r\cos\theta)^2 + c_1 \;\text{ if } (x - x_0) \leqslant -L \;\text{ or } (x - x_0) \geqslant L, \tag{A 4}$$

Considering symmetry across the θ-axis:

$$f_2(r) = \frac{c_1}{R^2}(r\cos\theta)^2 + c_1 \;\text{ if } (x - x_0) \leqslant -L \;\text{ or } (x - x_0) \geqslant L. \tag{A 5}$$

These profiles must satisfy the exact entry flow rate of each branch. Therefore, we refer to the definition of flow rate Q in order to find constant c_1

$$Q = \int_{-R}^{R}\int_{-L}^{L} f_1(x,y)\,dx\,dy + 2\int_{0}^{\pi}\int_{0}^{R} f_2(r) r\,dr\,d\theta,$$
$$c_1 = -\frac{Q}{\frac{8}{3}RL + \frac{\pi}{2}R^2}. \tag{A 6}$$

Replacing the value of c_1 on Eq.(A 2) and the cartesian version of Eq.(A 5), we obtain the inlet velocity profile for the cross-section considered in this study, illustrated in figure 10.

$$\mathbf{u}(x,y) = \begin{cases} \mathcal{A}\left(\dfrac{(y-y_0)^2}{R^2} - 1\right) & \text{if } |x - x_0| \leqslant L \\ \mathcal{A}\left(\dfrac{(x-x_0-L)^2}{R^2} + \dfrac{(y-y_0)^2}{R^2} - 1\right) & \text{otherwise,} \end{cases} \tag{A 7}$$

where $\mathcal{A} = \dfrac{-Q}{\frac{8}{3}RL + \frac{\pi}{2}R^2}$.

REFERENCES

Aicolina, LE, Leaver, IH & Stapleton, IW 1989 Fluorescence quenching studies of the self-association in ater of fluorescent surfactants. alkaryl-2-pyrazolines and alkyl-7-hydroxycoumarins. *Dyes and pigments* **11** (3), 213–232.

Antonopoulou, E, Harlen, O. G, Rump, M, Segers, T & Walkley, M. A 2021 Effect of surfactants on jet break-up in drop-on-demand inkjet printing. *Physics of Fluids* **33** (7), 72112.

Bastani, Dariush, Fayzi, Pouyan, Lotfi, Marzieh & Arzideh, Seyed Mahmoud 2018 Cfd simulation of bubble in flow field: investigation of dynamic interfacial behaviour in presence of surfactant molecules. *Colloid and Interface Science Communications* **27**, 1–10.

Carrier, O., Ergin, F. G., Li, H. Z., Watz, B. B. & Funfschilling, D. 2015 Time-resolved mixing and flow-field measurements during droplet formation in a flow-focusing junction. *Journal of Micromechanics and Microengineering* **25** (8), 084014.

Chen, Yang, Xu, Jian-Hong & Luo, Guang-Sheng 2015 The dynamic adsorption of different surfactants on droplet formation in coaxial microfluidic devices. *Chemical Engineering Science* **138**, 655–662.

Constante-Amores, C.R., Batchvarov, A., Kahouadji, L., Shin, S., Chergui, J., Juric, D. & Matar, O.K. 2021 Role of surfactant-induced marangoni stresses in drop-interface coalescence. *Journal of Fluid Mechanics* **925**, A15.

Dong, T., Weheliye, W. & Angeli, P. 2019 Laser induced fluorescence studies on the distribution of surfactants during drop/interface coalescence. *Physics of Fluids* **31**, 12106.

Dussaud, Anne D, Matar, Omar K & Troian, Sandra M 2005 Spreading characteristics of an insoluble surfactant film on a thin liquid layer: comparison between theory and experiment. *Journal of Fluid Mechanics* **544**, 23–51.

Eggeling, C., Widengren, J., Rigler, R. & Seidel, C. A. M. 1998 Photobleaching of fluorescent dyes under conditions used for single-molecule detection: Evidence of two-step photolysis. *Analytical Chemistry* **70** (13), 2651–2659.

Filimonov, Roman, Wu, Zan & Sundén, Bengt 2021 Toward computationally effective modeling and simulation of droplet formation in microchannel junctions. *Chemical Engineering Research and Design* **166**, 135–147.

Garstecki, Piotr, Stone, Howard A. & Whitesides, George M. 2005 Mechanism for flow-rate controlled breakup in confined geometries: A route to monodisperse emulsions. *Phys. Rev. Lett.* **94**, 164501.

Gassin, Pierre-Marie, Martin-Gassin, Gaelle, Meyer, Daniel, DufrÃªche, Jean-FranÃ§ois & Diat, Olivier 2012 Kinetics of triton-x100 transfer across the water/dodecane interface: Analysis of the interfacial tension variation. *The Journal of Physical Chemistry C* **116** (24), 13152–13160.

Van der Graaf, S, Nisisako, T, Schroën, CGPH, Van Der Sman, RGM & Boom, RM 2006 Lattice boltzmann simulations of droplet formation in a t-shaped microchannel. *Langmuir* **22** (9), 4144–4152.

Jin, Fang, Gupta, Nivedita R. & Stebe, Kathleen J. 2006 The detachment of a viscous drop in a viscous solution in the presence of a soluble surfactant. *Physics of Fluids* **18** (2), 022103.

Kahouadji, Lyes, Nowak, Emilia, Kovalchuk, Nina, Chergui, Jalel, Juric, Damir, Shin, Seungwon, Simmons, Mark JH, Craster, Richard V & Matar, Omar K 2018 Simulation of immiscible liquid–liquid flows in complex microchannel geometries using a front-tracking scheme. *Microfluidics and Nanofluidics* **22** (11), 1–12.

Kalli, M. & Angeli, P. 2022 Effect of surfactants on drop formation flow patterns in a flow-focusing microchannel. *Chemical Engineering Science* p. 117517.

Kalli, M., Chagot, L. & Angeli, P. 2022 Comparison of surfactant mass transfer with drop formation times from dynamic interfacial tension measurements in microchannels. *Journal of Colloid and Interface Science* **605**, 204–213.

Kamat, Pritish M, Wagoner, Brayden W, Thete, Sumeet S & Basaran, Osman A 2018 Role of marangoni stress during breakup of surfactant-covered liquid threads: reduced rates of thinning and microthread cascades. *Physical Review Fluids* **3** (4), 043602.

Kiratzis, I., Kovalchuk, N. M., Simmons, M. J. H. & Vigolo, D. 2022 Effect of surfactant addition and viscosity of the continuous phase on flow fields and kinetics of drop formation in a flow-focusing microfluidic device. *Chemical Engineering Science* **248** (B).

Kovalchuk, Nina M, Nowak, Emilia & Simmons, Mark JH 2017 Kinetics of liquid bridges and formation of satellite droplets: Difference between micellar and bi-layer forming solutions. *Colloids and Surfaces A: Physicochemical and Engineering Aspects* **521**, 193–203.

Kovalchuk, N. M., Roumpea, E., Nowak, E., Chinaud, M., Angeli, P. & Simmons, M. J. H. 2018 Effect of surfactant on emulsification in microchannels. *Chemical Engineering Science* **176**, 139 – 152.

Kovalchuk, Nina M & Simmons, Mark JH 2021 Effect of surfactant dynamics on flow patterns inside drops moving in rectangular microfluidic channels. *Colloids and Interfaces* **5** (3), 40.

Lan, Wenjie, Li, Shaowei, Wang, Yujun & Luo, Guangsheng 2014 Cfd simulation of droplet formation in microchannels by a modified level set method. *Industrial & Engineering Chemistry Research* **53** (12), 4913–4921.

Lawrence, M Jayne & Rees, Gareth D 2000 Microemulsion-based media as novel drug delivery systems. *Advanced drug delivery reviews* **45** (1), 89–121.

Leong, Chia Min, Gai, Ya & Tang, Sindy KY 2016 Investigating droplet internal flow in concentrated emulsion when flowing in microchannel using micro-piv. In *APS Division of Fluid Dynamics Meeting Abstracts*, pp. M25–003.

Li, Dongyang, Zhou, Li, Yu, Qiuhan, Pu, Xiaoyun, Sun, Yuze, Zhou, Qing & Zhang, Yuanxian 2022 Optical fiber optofluidic laser based on surfactant solubilization of rhodamine b gain in an aqueous solution. *Optics Express* **30** (13), 23295–23304.

Li, Xiao-Bin, Li, Feng-Chen, Yang, Juan-Cheng, Kinoshita, Haruyuki, Oishi, Masamichi & Oshima, Marie 2012 Study on the mechanism of droplet formation in t-junction microchannel. *Chemical Engineering Science* **69** (1), 340–351.

Martin, Jeffrey D & Hudson, Steven D 2009 Mass transfer and interfacial properties in two-phase microchannel flows. *New Journal of Physics* **11** (11), 115005.

Miessner, Ulrich, Helmers, Thorben, Lindken, Ralph & Westerweel, Jerry 2020 μpiv measurement of the 3d velocity distribution of taylor droplets moving in a square horizontal channel. *Experiments in Fluids* **61** (5), 1–17.

Muradoglu, Metin & Tryggvason, Gretar 2014 Simulations of soluble surfactants in 3d multiphase flow. *Journal of Computational Physics* **274**, 737–757.

Ngo, Ich-Long, Dang, Trung-Dung, Byon, Chan & Joo, Sang Woo 2015 A numerical

study on the dynamics of droplet formation in a microfluidic double t-junction. *Biomicrofluidics* **9** (2), 024107, arXiv: https://doi.org/10.1063/1.4916228.

Park, Daehwan, Kim, Hajeong & Kim, Jin Woong 2021 Microfluidic production of monodisperse emulsions for cosmetics. *Biomicrofluidics* **15** (5), 051302.

Pirbodaghi, Tohid, Vigolo, Daniele, Akbari, Samin & DeMello, Andrew 2015 Investigating the fluid dynamics of rapid processes within microfluidic devices using bright-field microscopy. *Lab on a Chip* **15** (9), 2140–2144.

Riaud, A., Zhang, H., Wang, X., Wang, K. & Luo, G. 2018 Numerical study of surfactant dynamics during emulsification in a t-junction microchannel. *Langmuir* **34** (17), 4980–4990.

Roumpea, E., Kovalchuk, N. M., Chinaud, M., Nowak, E., Simmons, M. J. H. & Angeli, P. 2019 Experimental studies on droplet formation in a flow-focusing microchannel in the presence of surfactants. *Chemical Engineering Science* **195**, 507–518.

Shin, Seungwon, Abdel-Khalik, SI, Daru, Virginie & Juric, Damir 2005 Accurate representation of surface tension using the level contour reconstruction method. *Journal of Computational Physics* **203** (2), 493–516.

Shin, Seungwon, Chergui, Jalel & Juric, Damir 2017 A solver for massively parallel direct numerical simulation of three-dimensional multiphase flows. *Journal of Mechanical Science and Technology* **31** (4), 1739–1751.

Shin, Seungwon, Chergui, Jalel, Juric, Damir, Kahouadji, Lyes, Matar, Omar K. & Craster, Richard V. 2018 A hybrid interface tracking – level set technique for multiphase flow with soluble surfactant. *Journal of Computational Physics* **359**, 409–435.

Shin, Seungwon & Juric, Damir 2002 Modeling three-dimensional multiphase flow using a level contour reconstruction method for front tracking without connectivity. *Journal of Computational Physics* **180** (2), 427–470.

Soh, Gim Yau, Yeoh, Guan Heng & Timchenko, Victoria 2016 Numerical investigation on the velocity fields during droplet formation in a microfluidic t-junction. *Chemical Engineering Science* **139**, 99–108.

Teipel, U. & Aksel, N. 2001 Adsorption behavior of nonionic surfactants studied by drop volume technique. *Chemical Engineering & Technology* **24** (4), 393–400.

Wang, K., Lu, Y.C., Xu, J. H & Luo, G.S. 2009 Determination of dynamic interfacial tension and its effect on droplet formation in the t-shaped microdispersion process. *Langmuir* **25** (4), 2153–2158.

Wang, K., Zhang, L., Zhang, W. & Luo, G. 2016 Mass-transfer-controlled dynamic interfacial tension in microfluidic emulsification processes. *Langmuir* **32** (13), 3174–3185.

Wilke, CR & Chang, Pin 1955 Correlation of diffusion coefficients in dilute solutions. *AIChE journal* **1** (2), 264–270.

Xu, J. H., Dong, P. F., Zhao, H., Tostado, C. P. & Luo, G. S. 2012 The dynamic effects of surfactants on droplet formation in coaxial microfluidic devices. *Langmuir* **28** (25), 9250–9258.

Xu, J. H., Luo, G. S., Li, S. W. & Chen, G. G. 2006 Shear force induced monodisperse droplet formation in a microfluidic device by controlling wetting properties. *Lab Chip* **6**, 131–136.

Yang, Lisong, Kapur, Nik, Wang, Yiwei, Fiesser, Fritz, Bierbrauer, Frank, Wilson, Mark C.T., Sabey, Tim & Bain, Colin D. 2018 Drop-on-demand satellite-free drop formation for precision fluid delivery. *Chemical Engineering Science* **186**, 102–115.

Zhao, Shufang, Riaud, Antoine, Luo, Guangsheng, Jin, Yong & Cheng, Yi 2015 Simulation of liquid mixing inside micro-droplets by a lattice boltzmann method. *Chemical Engineering Science* **131**, 118–128.